Journal of Marine Research, 57, 245–274, 1999

Lagrangian statistics in unforced barotropic flows

by J. H. LaCasce[1,2] and K. G. Speer[1]

ABSTRACT

We consider the dispersion of particles in potential vorticity (PV)-conserving flows. Because particle drift is preferentially along the mean PV contours, Lagrangian dispersion is strongly anisotropic. If the mean PV field moreover is spatially variable, as when there is topography, the anisotropy is more clearly visible in the dispersion of displacements along and across the mean PV field itself. We examine several numerical examples of unforced barotropic flows; in all cases, this "projected" dispersion is more anisotropic than that in cartesian (x, y) coordinates. What differs is the rate at which spreading occurs, both along and across contours. The method is applicable to real data, as is illustrated with float data from the deep North Atlantic. The results suggest a preferential spreading along contours of (barotropic) f/H.

1. Introduction

Particle transport in turbulent flows is often idealized as a diffusive process, following the landmark work of Taylor (1921). Taylor imagined a random walk-type motion which might occur in isotropic, homogeneous turbulence, and showed how such a process would lead to a diffusion of particles in x and y. This idea has been refined and applied to the interpretation of oceanic float data (Davis, 1991). Davis's modifications allow for a spatially variable, possibly anisotropic diffusivity and for a variable mean flow, both of which are determined by direct measurements. Though sophisticated, the foundation of such a construction nevertheless is the assumption of lateral diffusion.

However, the ocean, with rotation, stratification, bottom topography and mean flows is not necessarily as simple as homogeneous turbulence. How will such elements affect particle dispersion? In the absence of forcing, fluid parcels move in such a way as to conserve their potential vorticity (PV), e.g. Pedlosky (1987); as such, they will resist drifting *across* mean PV contours, and one thus expects that tracer spreading will be preferentially parallel to the mean PV field. All of the aforementioned elements (stratification, etc.) could alter the mean PV, and therefore affect Lagrangian dispersion.

The difficulty is in knowing which elements are important. If one knew the relative strengths of the (stratified) wind-driven circulation, barotropic and baroclinic eddies, and all other dynamical elements, one could make an educated guess. An alternative would be

1. IFREMER, Centre de Brest, Lab de Physique des Oceans, BP 70, 29280 Plouzane, France.
2. Present address: Woods Hole Oceanographic Institution, Woods Hole, Massachusetts, 02543, U.S.A. ***email:jlacasce@whoi.edu***

to examine actual particle trajectories vis a vis chosen mean PV fields, and look for correlations. The latter is the approach of the present work, and in particular, we define a rudimentary means of quantifying this correlation: the Lagrangian dispersion relative to the PV field itself. Such a measure is useful because it will reveal whether dispersion is more anisotropic relative to the mean PV field than in x and y. In addition, the rates of increase of the dispersion along and across contours is found; thus one discovers for example whether the spreading is consistent with lateral diffusion.

In the present work, we examine dispersion in some idealized examples. For simplicity, we focus on unforced barotropic flows, where particles conserve their total PV:

$$q = \frac{\nabla^2\psi + f(y)}{H(x, y)}, \tag{1}$$

where $H(x, y)$ is the water depth, $\psi(x, y)$ is the streamfunction which defines the velocity field and $f(y)$ is the Coriolis parameter. For quasi-geostrophic flows (such as those discussed hereafter), the variation of water depth is order Rossby number, and the mean PV may be written:

$$\overline{q} = f_0 + \beta y + \frac{f_0}{H_0} h(x, y) \tag{2}$$

where $H(x, y) = H_0 - h(x, y)$ and $|h| \ll |H_0|$ (Pedlosky, 1987), and the β-plane approximation (f is a linear function of y) has been made. The mean portion of the PV field is the so-called *f/H* field (the *f/H* contours discussed subsequently are defined as in (2)), and because motion across these contours must be balanced by changes in relative vorticity ($\nabla^2\psi$), so we expect long term particle drift to be aligned with *f/H*.

If the bottom is flat, or $H = const.$, zonal drift is favored over meridional drift, due to the β-effect. This tendency will be clearly visible as an anisotropy between the zonal and meridional dispersions (the mean square distance from the particle starting positions). If the bottom is not flat, and moreover if the topography varies in both directions ($H = H(x, y)$), the anisotropy may not necessarily be evident with the Cartesian dispersion; rather one ought to examine the dispersion of displacements along and across *f/H*.

Hereafter, we consider a hierarchy of barotropic flows: a single Rossby wave, multiple Rossby waves, turbulence on the β-plane and turbulence over topography. In all cases, one observes anisotropic dispersion; what differs is the rate of spreading, which in these cases depends on the number of significant Eulerian components (waves, mean flows, etc.). In a later work (LaCasce and Speer, 1999) we examine whether oceanic floats are sensitive to barotropic *f/H*. The results of one calculation, for floats in the deep North Atlantic, is presented here for comparison. All statistical quantities discussed are presented in the Appendix.

2. Rossby waves

Arguably the simplest geophysical example of particle transport is that of particles advected by a finite amplitude Rossby wave in a channel. Such a wave is a solution of the

quasi-geostrophic PV equation, i.e.

$$\frac{\partial}{\partial t}\nabla^2\psi + J(\psi, \nabla^2\psi) + \beta\frac{\partial}{\partial x}\psi = 0, \tag{3}$$

under the condition of vanishing flow at $y = 0$ and $y = 2\pi$. The function $J(a, b) \equiv (\partial a/\partial x\, \partial b/\partial y) - (\partial b/\partial x\, \partial a/\partial y)$, is the Jacobian. A wave solution, which is also an exact solution of (3), is:

$$\psi = A\cos(kx - \omega t)\cos(ly), \qquad \text{with } \omega = \frac{-\beta k}{k^2 + l^2}; \tag{4}$$

this streamfunction defines a velocity field which in turn may be used to advect particles. Regier and Stommel (1979) numerically calculated such trajectories and showed that the particles drift along latitude lines. Flierl (1981) derived analytical expressions for this Lagrangian drift, both in the case of small amplitude waves (for which the Stoke's approximation is appropriate) and for large amplitude waves (for which it is not). The reader is referred to Flierl (1981) for examples of trajectories and details on the method of solution. Flierl showed that:

$$u_D = f(\varepsilon, x, y) \tag{5}$$

where $\varepsilon \equiv U/c$ is the ratio of the wave advective velocity to the phase velocity. The drift velocity is *either* eastward or westward (see the lower panel of Fig 3), despite the fact that the wave phase speed is uniquely westward, and varies in *both* x and y. At small ε, $u_D \alpha \varepsilon^2$; with $\varepsilon > 1$, the eastward drift velocity increases linearly with ε, but the westward velocity is bounded by c, the wave phase speed. Particles moving westward at $u_D = c$ are trapped by the wave, whereas the eastward particles are expelled in the opposite direction. For values of $\varepsilon < 5$, approximately equal numbers of particles move west and east (assuming a uniform initial deployment). At larger values of ε, more and more particles are trapped by the wave and so move westward.

Particles advected by a single wave therefore experience zonal shear dispersion. That is to say that their mean separation from their starting meridian increases quadratically in time, because:

$$\langle (x - x_0)^2 \rangle = \langle u_D(x, y)^2 \rangle t^2, \tag{6}$$

where the brackets denote an average over all particles (see comments in the Appendix). The quadratic time dependence occurs for all wave amplitudes. From the above, one expects the total dispersion to scale with ε^4 (i.e., proportional to the square of the kinetic energy) for weak waves ($U < c$); for strong waves ($U > c$), the dispersion should increase less rapidly than quadratically with (ε), assuming that not all particles are trapped by the wave.

Meridional dispersion on the other hand is bounded because particles periodically return

to their starting latitude, from (4). If the Lagrangian period were identical for all particles, the meridional dispersion would collapse to zero at every period, but like the drift velocity, the Lagrangian period also depends on the initial position (Flierl, 1981). One observes that the meridional dispersion saturates at a constant positive value (see Fig. 1). The time at which saturation occurs is indicative of the mean Lagrangian period.

The principal point is that particles in a single Rossby wave experience anisotropic spreading: shear dispersion in the zonal direction, and bounded dispersion in the meridional direction. The Rossby wave differs from a shear flow primarily because particles deployed at the same latitude may move either east or west.

Because the Lagrangian drift varies with a particle's position in the wave, if one displaces the particle, the drift rate will change. Thus a second Eulerian component, such as a second wave or a mean shear, can alter the rate of spreading. Here we examine the former case, i.e. of adding a second wave. Similar two-wave systems have been considered for example by Weiss and Knobloch (1989) and Pierrehumbert (1991), both of whom studied the chaotic mixing obtained upon the addition of the second wave.

Like Pierrehumbert, we assume the additional wave is of similar zonal extent, but of half the meridional extent; the results depend only weakly on this choice. By the Rossby wave dispersion relation, the secondary wave has a slower phase speed, and the streamfunction then has the following form:

$$\psi = A \cos(x - c_1 t) \cos(y) + A_2 \cos(x - c_2 t) \cos(2y), \tag{7}$$

where $|c_2| = 1/5 < |c_1| = 1/2$. We gauge the secondary wave strength by $\varepsilon_2 = U_2/c_2$; the primary wave is assumed to have $\varepsilon_1 = U_1/c_1 = 1$. Particles were advected via a fourth-order Runge-Kutta scheme, and the dispersions (defined in the Appendix) for different combinations of waves are shown in Figure 1.

At early times, the dispersion in both directions increases quadratically in time, as predicted by Taylor (1921). Later on, the anisotropy between zonal and meridional spreading is evident, and the meridional dispersion in particular is bounded. The latter is expected because the meridional velocity for both waves vanishes at $y = 0$ and $y = 2\pi$, so no particles can pass these latitudes. The rate of zonal spreading on the other hand depends on the relative strengths of the waves. If the smaller wave is very weak, we recover the single wave dispersion which increases quadratically in time (solid line). When the waves are comparable in strength, the increase is more nearly linear in time, as it would be for a diffusive process (Taylor, 1921). If the smaller wave is much stronger, the dependence is again nearly quadratic; i.e., as if there were only one wave. In other words, shear dispersion is found if one wave dominates, otherwise the rate of increase is less than quadratic.

As discussed by Weiss and Knobloch (1989) and Pierrehumbert (1991), a second wave permits chaotic mixing. For our purposes, the second wave permits particles to access different parts of the primary wave, and thereby drift zonally at different speeds. In the limit of a weak secondary wave, particles are only marginally displaced from their original positions, but if the second wave is strong, the particles may wander into all regions of the

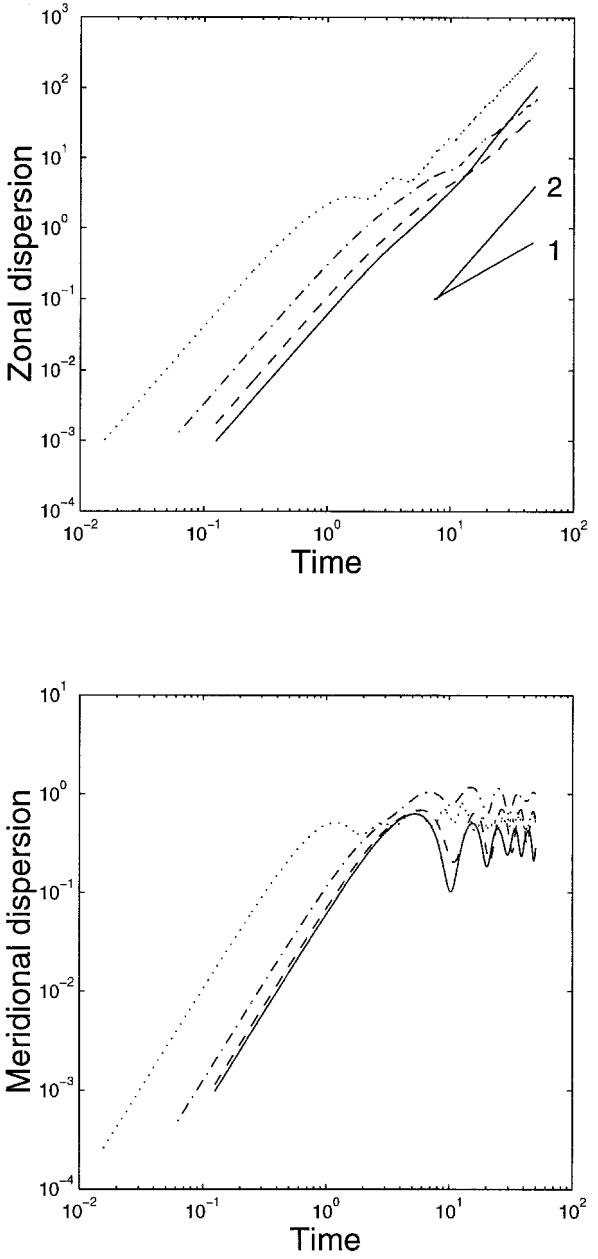

Figure 1. Dispersion (as defined in the Appendix) of particles advected by a superposition of two Rossby waves. Zonal dispersion is shown in the upper panel, meridional dispersion in the lower. The different curves correspond to different amplitudes of the second (smaller) wave; $\varepsilon_2 \equiv U_2/c_2 = 0$ (solid), $\varepsilon_2 = .5$ (dashed), $\varepsilon_2 = 2$ (dash-dot) and $\varepsilon_2 = 10$ (dots).

primary wave. In other words, the flow becomes *ergodic*. As discussed for example by Mezic and Wiggins (1994), there is a significant connection between ergodicity and diffusive dispersion.

There are, however, other interesting aspects about this two-wave case. The greatest zonal dispersion occurs when the smaller wave is strong ($\varepsilon_2 = 10$). In this case, the second wave dominates advection, and the large dispersion is caused by the rapid eastward expulsion (at speeds greater than the wave phase speed). Secondly, the meridional dispersion saturates at an *earlier* time when the smaller wave dominates, suggesting a smaller mean Lagrangian period. This is curious, because the smaller wave period is actually longer. However, the important time scale in the limit of a strong wave is the wave *advective* time scale, L_y/U_2.

The primary point is that the rate of spreading along the mean PV contours depends on the number and relative strengths of the advecting components. The caveat in this case is that a dynamically consistent model with two Rossby waves would be nonstationary, because two Rossby waves can interact nonlinearly to produce additional waves. Nevertheless, the results are useful in understanding dispersion under actual solutions of Eq. (3), as in the following sections.

3. β-turbulence

We seek a multi-component flow which is a solution of Eq. (3). One approach would be to initialize a numerical model with two waves and let them evolve in time, as was done by Pierrehumbert (1991). An alternative is to consider many interacting modes, i.e. a turbulent flow. Energy in freely evolving turbulence in two dimensions shifts to larger scales, the so-called "inverse cascade" (e.g. Fjortoft, 1953; Kraichnan and Montgomery, 1980). With β, the cascade slows greatly at a certain scale, due to competition from Rossby waves which are relatively inefficient at energy transfer (e.g. Rhines, 1975). Thereafter, the evolution is very slow, slow enough to be quasi-stationary for our purposes. Particle motion in forced β-turbulence has been considered previously (Holloway and Kristmannsson, 1984), but while forcing and dissipation permit statistically stationary solutions, PV is no longer conserved if the flow is barotropic. So we necessarily focus on unforced turbulence.

We begin with an initial flow with random phases and an energy spectrum defined by:

$$KE_1(\kappa) = \begin{cases} 0 & \text{if } \kappa < \kappa_0 \\ \dfrac{KE_{01}\kappa^6}{(\kappa + \kappa_0)^{18}} & \text{if } \kappa \geq \kappa_0 \end{cases}$$

where $\kappa = (k^2 + l^2)^{1/2}$ is the total wavenumber and $\kappa_0 = 14$. With $\beta = 64$, the arrest scale (Rhines, 1975) is roughly one sixth the domain scale, which has a nondimensional value of 2π. So if the domain were 1100 km × 1100 km, the initial scale would be about 75 km, and the arrest scale about 200 km.

The solution was calculated with a doubly periodic spectral code with 256^2 Fourier modes, described in Flierl (1994) and LaCasce (1998). Two points should be emphasized. Firstly, one may model flow on the β-plane while retaining meridional periodicity because only the gradient (β) enters in Eq. (3). Secondly, the model has a numerical filter which damps large wavenumbers, so potential vorticity is not conserved; PV rather is removed at small scales, similar to a very scale-selective diffusion. One thus expects deviations from inviscid dynamics, but the apparent effects are small.

The horizontal wavenumber spectra at three different times are shown in Figure 2. The energy is seen to shift to graver scales, and arrest at mode $(k, l) = (1, 4)$. The spectra evolves only gradually between $t = 50$ and $t = 150$, justifying the assumption of quasi-stationarity. Note the dominant mode, $(k, l) = (1, 4)$, is a "wave" mode not a "jet" mode ($k = 0$), the arrested state commonly found for forced turbulence (e.g. Vallis and Maltrud, 1994); consistent with this, one observes westward phase propagation in successive streamfunction plots (not shown), as with a single wave.

A number of particles ($N = 441$) were seeded uniformly in the domain at $t = 50$, a time well after the arrest. The particles were advected via a fourth order interpolation scheme; trajectories for a representative subset ($N = 44$) of particles are shown in the upper panel of Figure 3. While individual trajectories are complex (magnified view in insert), most particles exhibit a systematic zonal drift. The direction of drift depends on the initial position, with some moving west and others east.

For comparison, we made a single wave kinematic calculation with a streamfunction amplitude approximately equal to that found at harmonic (1, 4) (Fig. 2), the same wave scale and the same value of β; we obtain $\varepsilon \approx 0.13$ (Section 2), so the arrested wave is "weak" in the sense of Section 2. The resulting trajectories are shown in the lower panel of (3). Unlike in the turbulence case, these are smooth and periodic (see insert). However, the particles also drift zonally, and the dispersion (Fig. 4) is nearly the same; i.e., shear dispersive in the zonal direction and bounded meridionally.

So arrested turbulence behaves like a single Rossby wave, in terms of particle advection. Though other modes are present (Fig. 2), they are too weak to alter systematically the Stokes drift associated with the (1, 4) mode. In other words, particles are not "bumped" into different regions of the primary wave, and so do not change the direction of zonal drift. As with a single wave (Flierl, 1981), the direction of drift depends on the initial latitude and longitude of the particle.

Unlike in the kinematic wave case, the meridional velocity here does not vanish at some latitude, nevertheless meridional dispersion ceases. This is a consequence of the conservation of potential vorticity. On the β-plane, both the relative enstrophy ($\int\int |\nabla^2\psi|^2 \, dA$) and the potential enstrophy ($\int\int |\nabla^2\psi + \beta y|^2 \, dA$) are conserved (e.g. Rhines, 1977); this in turn bounds meridional displacements, because if particles continued to spread in y, their total enstrophy would have to increase to balance the displacements.

We note that Pierrehumbert's (1991) final state was also dominated by a single wave, so the present solution is similar, despite greatly different initial conditions; however, this is to

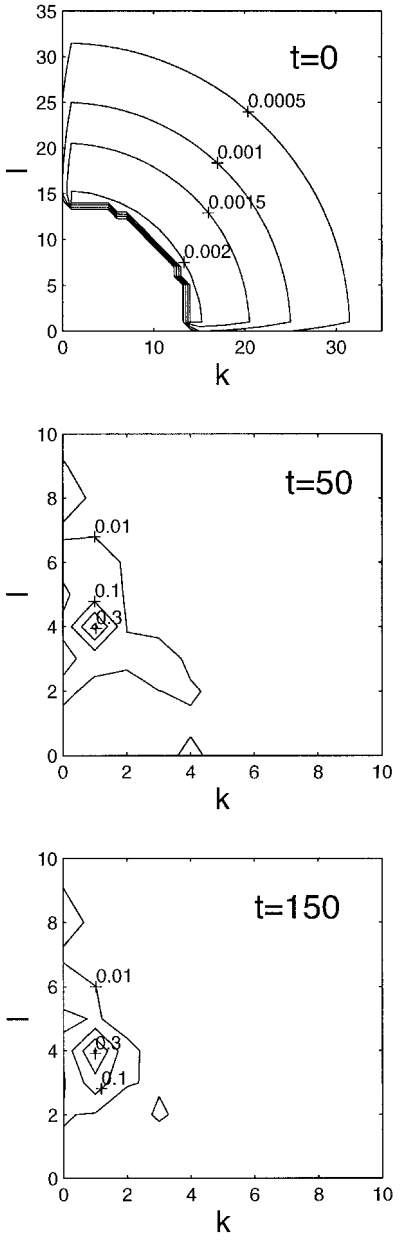

Figure 2. The horizontal wavenumber spectra, $E(k, l) = (k^2 + l^2)\,|\psi(k, l)|^2$, from the β turbulence runs at three different times. The values of the contours are as indicated.

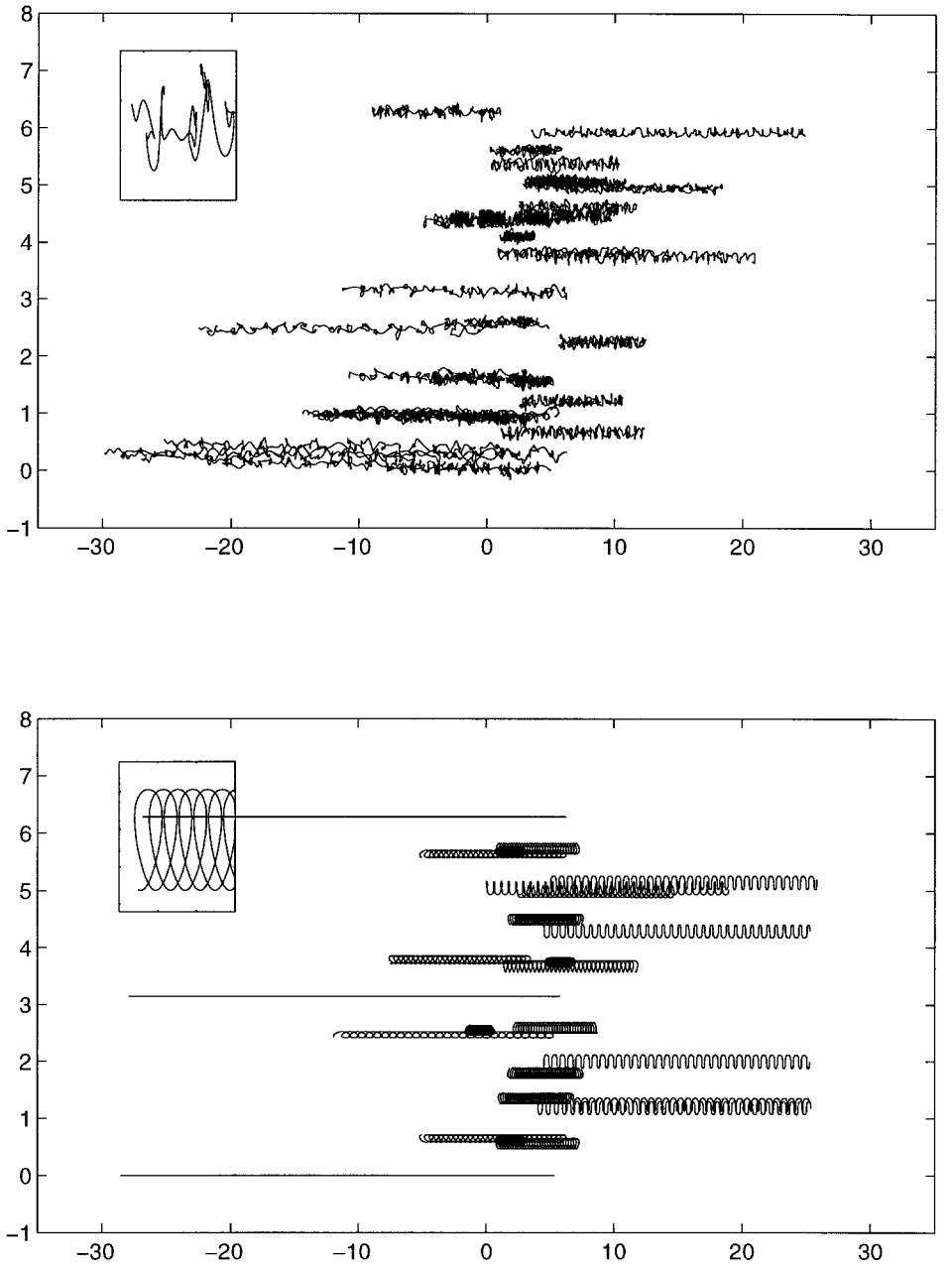

Figure 3. Particle trajectories from the β turbulence case (upper panel) and from a single wave kinematic model (lower). A magnified portion of the trajectories in each case are shown in the inserts.

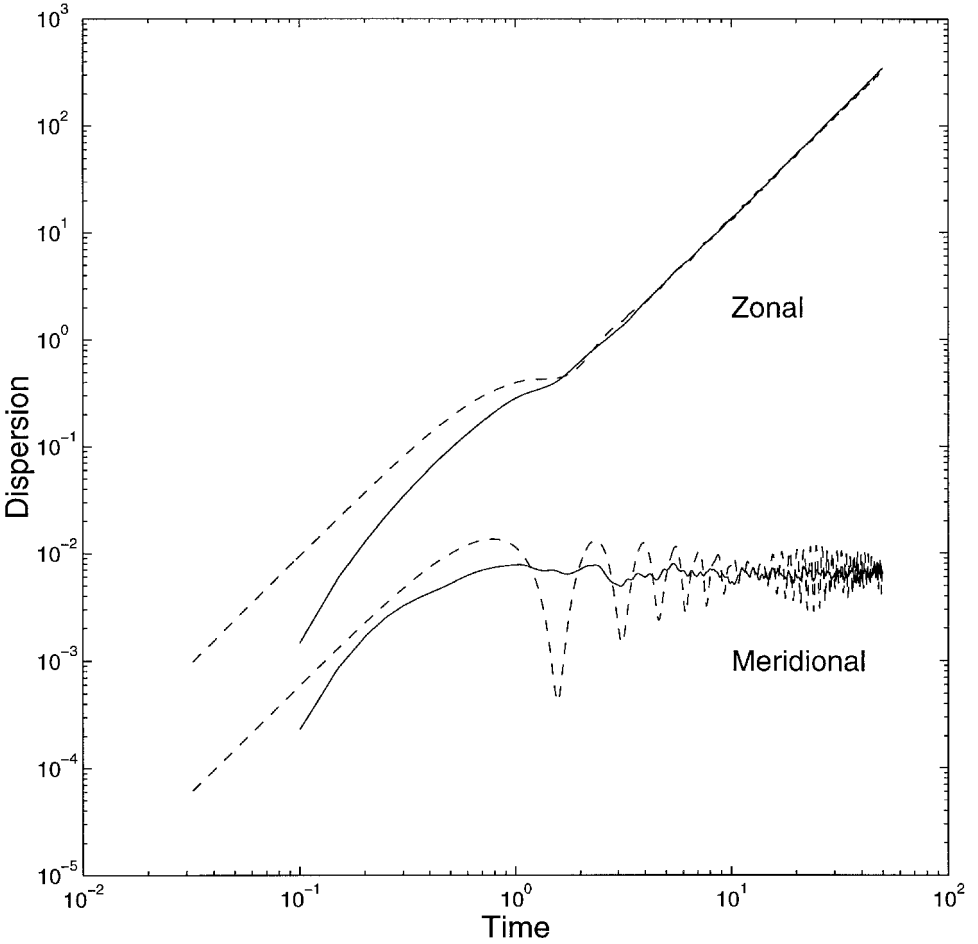

Figure 4. Particle dispersion for the β turbulence case, with comparable curves for a single wave kinematic experiment. The wave had an amplitude of $\varepsilon_1 = U_1/c_1 = .13$ and wavenumbers $(k, l) = (1, 4)$.

be expected, given an inverse cascade. Our value of β is somewhat larger, producing a smaller scale final state, but otherwise the difference is not great. While Pierrehumbert did not calculate dispersion, the result likely would have been similar to that found here.

In addition, the agreement with the purely inviscid, single-wave case reassures us that numerical dissipation in the β-turbulence case is of little consequence, at least on these time scales. This is probably because energy (which resides at large scales) is nearly conserved after the deployment of the particles.

4. Ridges

Now we turn to cases in which the mean PV is not oriented parallel to latitude lines; the previous experiment is repeated, but with topography. The topography was taken to vary

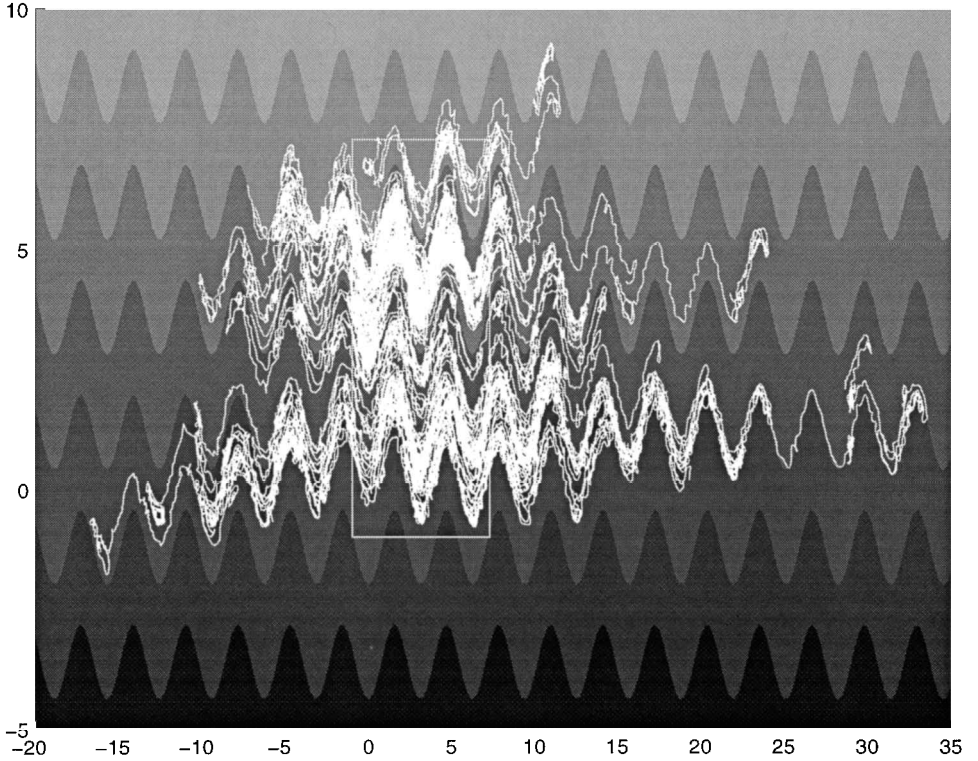

Figure 5. Trajectories for the ridge case, superimposed on *f*/*H*. The particles were deployed in the area indicated by the white box.

sinusoidally in the zonal direction, so that the (variable portion of the) mean PV is:

$$\overline{q} = \beta y + h = \beta y + h_0 \cos(x). \tag{8}$$

We take $\beta = 64$ and $h_0 = 50$; the latter was chosen so that the topography and βy were comparably strong. The resulting contours of *f*/*H* are open and undulating, as seen in Figure 5.[3] The initial flow used in Section 3 was allowed to evolve freely and arrest, and then particles were deployed. The trajectories of a subset are shown in Figure 5. One notes a zonal spreading, as in the previous case, but preferentially along the *f*/*H* contours.

In the β turbulence case, the arrested state was wave-like, and zonal mean flows were at best weak (Fig. 2). In contrast, there is a significant mean flow with the ridges (upper panel of Fig. 6). The flow has narrow jets oriented "eastward" relative to the *f*/*H* field, and broader "westward" return flows (similar asymmetric flows have been discussed by Rhines, 1977). In addition, there is a comparably strong wave component which makes the

3. The *f*/*H* field shown represents the periodic topography plus βy, and so the field appears periodic only in x. This was done merely for visual purposes, but is irrelevant to the dynamics which depend only on the mean gradient of PV.

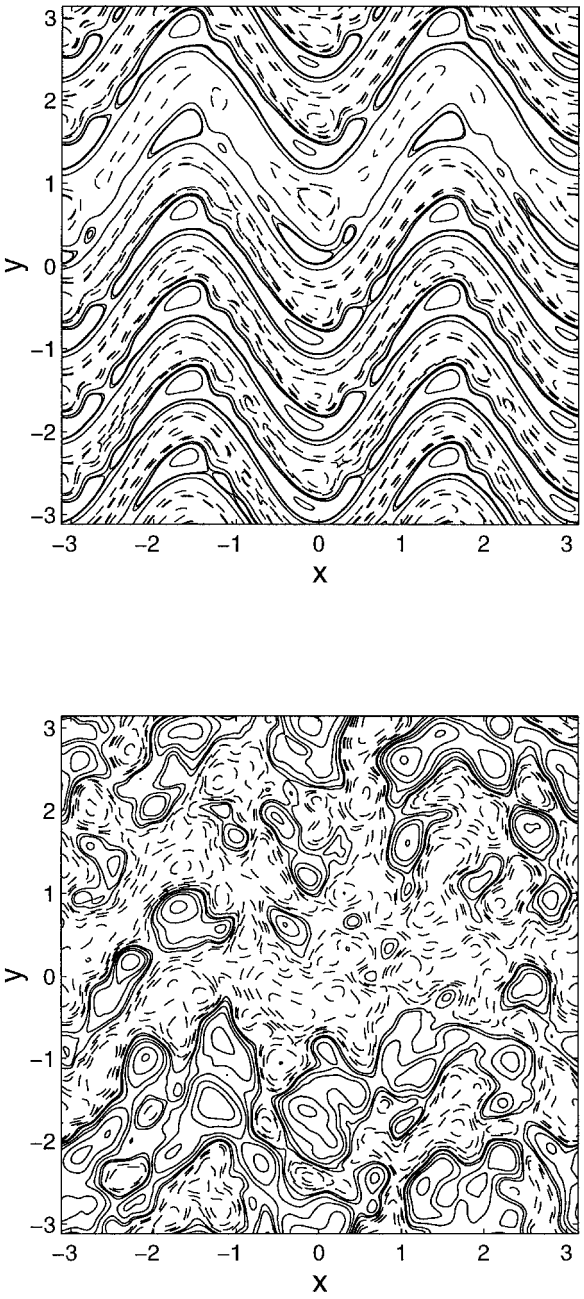

Figure 6. The mean (upper panel) and instantaneous (lower panel) streamfunctions for the ridge case. The instantaneous field is from $t = 7.5$. The contour values are [.025, .05, .15, .25, .35, .45], and dashed contours correspond to negative values.

mean flow difficult to see in plots of the instantaneous streamfunction (lower panel of Fig. 6). The nondimensional rms mean velocity is 0.52, whereas the rms total velocity is 0.94.

The mean dispersion in zonal and meridional directions is plotted in the upper panel of Figure 7. The preference for zonal spreading is seen after $t = 5$, and the increase in the zonal dispersion is approximately linear in time, suggestive of zonal diffusion (see below). The dispersion in y increases much more slowly, and nearly ceases at late times.

As can be inferred from Figure 6, neither the mean flow nor the wave phase speeds are oriented east-west, but rather along the f/H contours. So one is tempted to consider the dispersion of displacements *relative* to the f/H contours; the method for calculating such displacements is given in the Appendix; the results are shown in the lower panel of Figure 7. Plotted are (D_ζ, D_η), the dispersion of displacements along and across f/H contours respectively. The third curve indicates $D_{f/H}$, the dispersion of Lagrangian f/H itself; i.e., of the values of f/H seen at each instant by the particles. The latter is calculated here basically as a check for the cross contour dispersion (see Appendix).

One observes first that dispersion along f/H contours is several orders of magnitude larger than that across, so dispersion is more anisotropic relative to f/H than it is in Cartesian coordinates. Moreover, $D_\zeta > D_x$ at any given time, so the distance travelled along f/H is greater than in x. Similarly the cross contour dispersion is also less than that across latitude lines, suggesting a greater resistance to crossing f/H contours.

Like the zonal dispersion, D_ζ increases linearly in time. Such a linear increase is usually indicative of a normal distribution of displacements, as is the case here, and of diffusion (e.g., Batchelor and Townsend, 1953). So the motion is statistically equivalent to a diffusive spreading along f/H. Had there only been the mean flow, one would expect to recover shear dispersion; the diffusion is evidently due to the additional advection by the strong wave component (Fig. 6) which forces particles across the mean streamlines. Indeed, particles are found to reverse their drift direction frequently.

As noted, the dispersion across f/H is also increasing in time; this is not an error of the projection process (Appendix) because the dispersion about the initial value of f/H, $D_{f/H}$, is also increasing in time. In fact, both measures grow approximately linearly with t, suggesting diffusion across contours as well, albeit markedly less than along the contours. However the dispersion across latitude lines has apparently ceased; why is this? The conservation of potential vorticity (1) guarantees the conservation of potential enstrophy, which we may rewrite as follows:

$$\int\int (\tfrac{1}{2})(\nabla^2\psi + h + \beta y)^2 = \int\int (\tfrac{1}{2})(\nabla^2\psi + h)^2 + \int\int \beta y \nabla^2\psi + \int\int \beta y\, h + \int\int (\tfrac{1}{2})\beta^2 y^2. \tag{9}$$

The last two terms on the right are constants of the domain, and the second term on the right, proportional to Kelvin's impulse, is conserved in a doubly periodic domain; so the first term on the right is also constant. Because both the full potential enstrophy and that

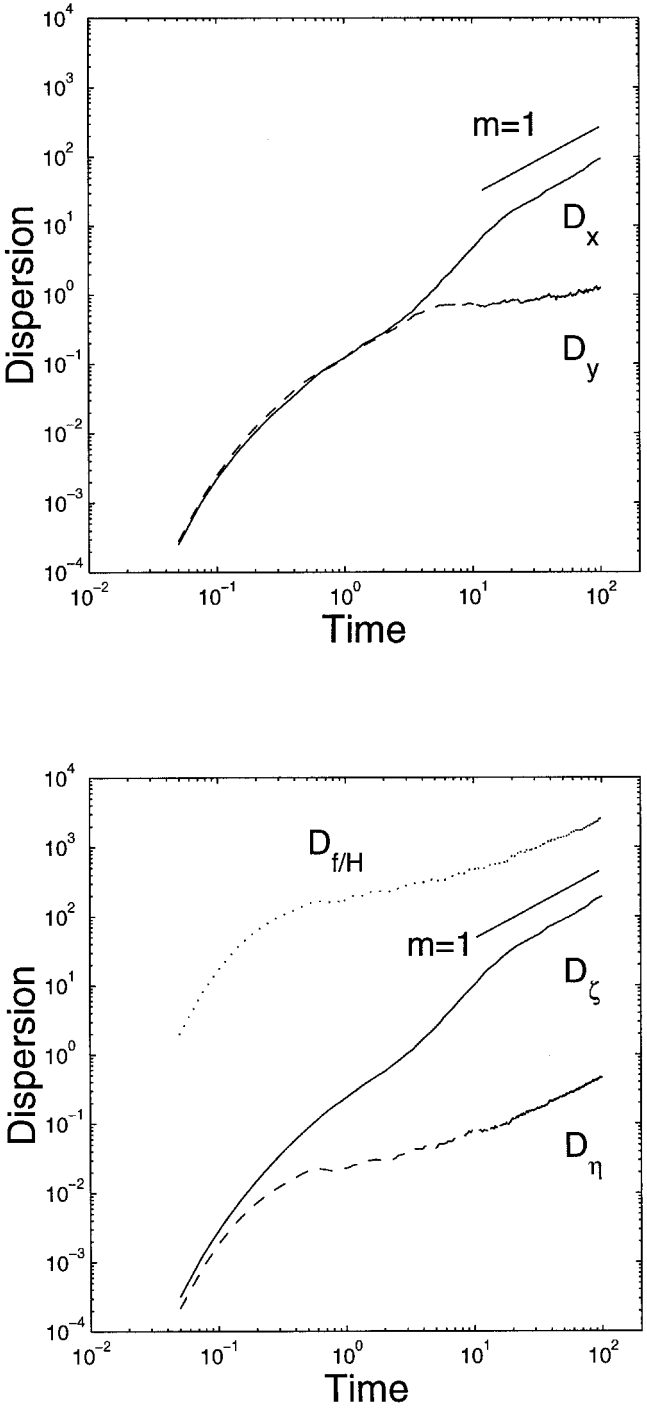

Figure 7. Dispersion in the ridge case. The zonal and meridional dispersion are shown in the upper panel, the dispersion relative to f/H in the lower panel. Also shown in the lower panel is the dispersion of values of f/H sampled by the particles, $D_{f/H}$.

portion without βy are separately conserved, we may infer a bound on meridional displacements of particles, just as when the bottom was flat.

In contrast enstrophy, $(\frac{1}{2})|\nabla^2\psi|^2$, is not separately conserved (as noted by Rhines, 1977), so we cannot deduce a similar bound on $(\beta y + h)$. In practice, however, the Lagrangian variance, $D_{f/H}$, is bounded because the meridional spread is bounded and because the topography is periodic in x; the bound is the maximum of $(|\Delta\ (\beta y + h)|_{\max})^2$ in a zonal band of a width determined by the meridional spread, here about one unit. That value is about 3×10^4, which is larger by an order of magnitude than the observed value of $D_{f/H}$ at $t = 100$. Of interest is that the bound on meridional spreading is reached before that across f/H, suggesting in turn a greater reluctance for drifting across f/H.

We have neglected the possibility that the topography itself might have a large-scale gradient, which in turn would act like β to limit dispersion across the gradient. If for example, $h = h' + \alpha x$, one could separate out the linear portion and argue for a cessation in zonal spreading. Such might be the case with a meridionally-oriented continental slope.

The main point is that dispersion is more anisotropic with respect to f/H than in conventional cartesian coordinates, and that this is to be expected, given conservation of PV. However, the difference between the dispersions in this case is not great, because the f/H contours are mostly open. A more striking difference is found when the contours are closed, as seen next.

5. Bumps

Next we take the mean PV field to be:

$$\beta y + h = 32.0y + 40.0 \cos(x) \cos(y). \tag{10}$$

Again particles were deployed after the spectral evolution had slowed; a subset of the trajectories and the f/H field are shown in Figure 8. Many particles appear trapped in regions of closed f/H contours, but some execute long, winding paths in open contour regions. The particle motion is reminiscent of that found in the laboratory experiments of Solomon *et al.* (1993), in which the Eulerian flow was dominated by large vortices between concentric cylinders. Their particles circled the vortices, but occasionally escaped and moved in the outer perimeter, around the vortices. Such "Levi flights" are associated with "anomalous," or nondiffusive, dispersion, and consistent with this, the zonal dispersion in our case (upper panel of Fig. 9) increases as $t^{1.5}$; i.e., is neither shear dispersive nor diffusive. The meridional dispersion appears eventually to cease.

Projecting the displacements onto f/H and recalculating the dispersion, one obtains the curves in the lower panel of Figure 9. As in the topographic ridge case, the dispersion anisotropy is evident at earlier times with the projected displacements, and the spread across f/H contours is less than that across latitude lines. Interestingly, the results suggest $D_\zeta \propto t^2$, or that the along-contour motion is approximately shear dispersive. Given the results of the previous sections, one might infer a strong mean flow or single wave, oriented along f/H contours. Again the cross contour dispersion increases throughout the duration of

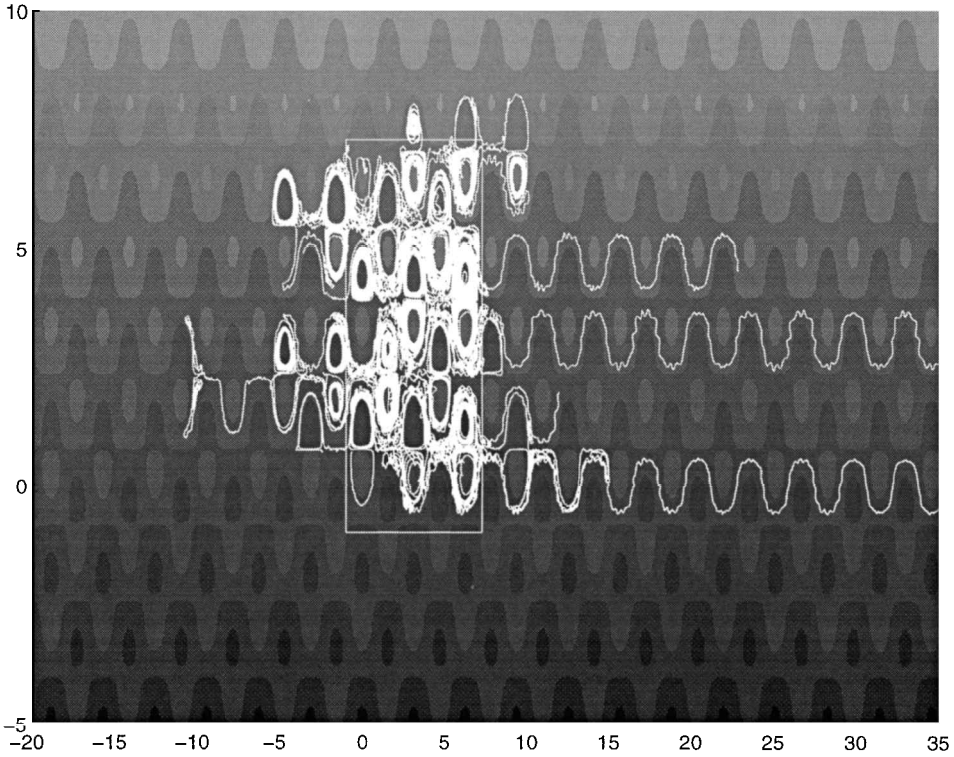

Figure 8. Trajectories for the cosine bump case, superimposed on *f*/*H*.

the experiment, although at a slower rate than over the ridges; one finds that $D_\eta \propto t^{.35}$ at late times.

Plots of the mean streamfunction (upper panel of Fig. 10) confirm the presence of a strong mean flow whose streamfunction is anti-correlated with *f*/*H*. Moreover, the mean flow is the dominant dynamical element, as can be seen by comparing to the instantaneous streamfunction (lower panel of Fig. 10), or the rms mean velocity (0.86) to the instantaneous value (0.95) at late times. It is well known (e.g. Bretherton and Haidvogel, 1976; Holloway, 1978; 1992) that freely evolving turbulence over bumps develops a mean streamfunction which is anti-correlated with the topography.[4] In the present case the mean dominates the late flow, as well as the particle dispersion.

Projecting displacements onto *f*/*H* has thus removed anomalous dispersion. The reason simply is that all particles are drifting at different speeds along *f*/*H* contours, whether in regions of closed or open contours. The total dispersion in the projected frame is much greater than in the zonal direction, because particles circulating around closed contours contribute to the net along-contour displacement, even though they have effectively ceased

4. The flow has been called the "Neptune effect" by Holloway (1992).

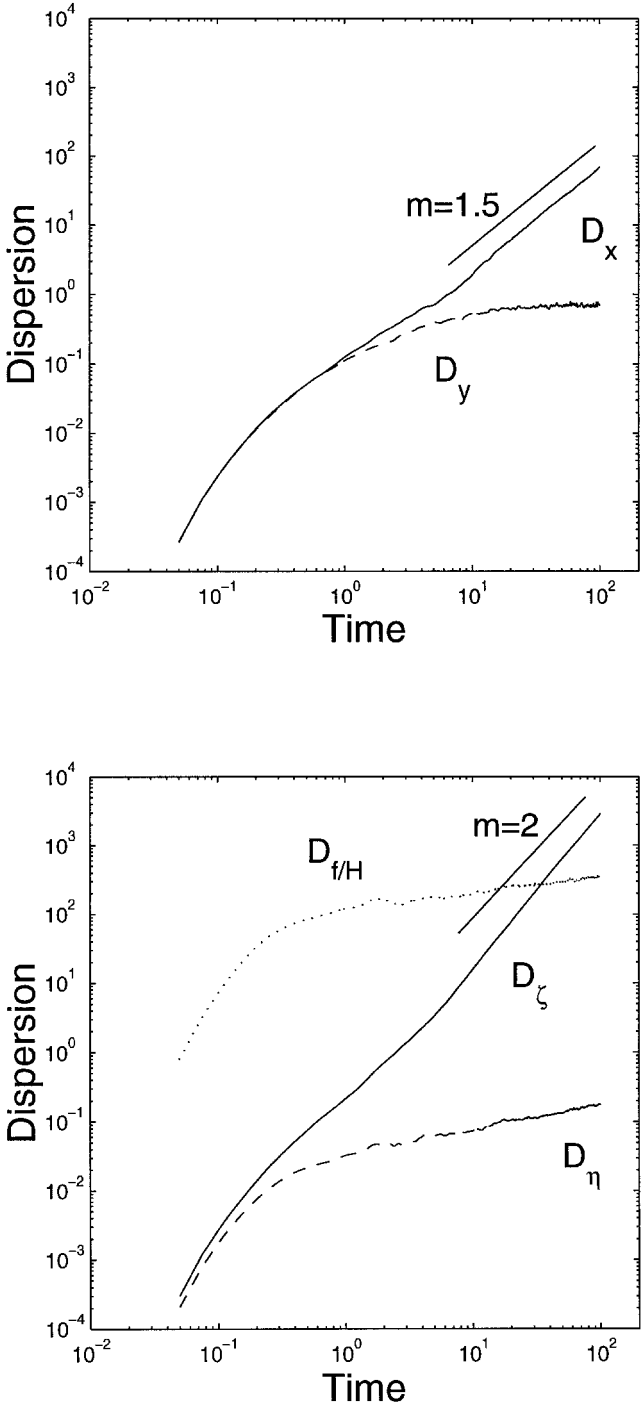

Figure 9. Dispersion in the cosine bump case. The zonal and meridional dispersion are shown in the upper panel, the dispersion relative to f/H in the lower panel.

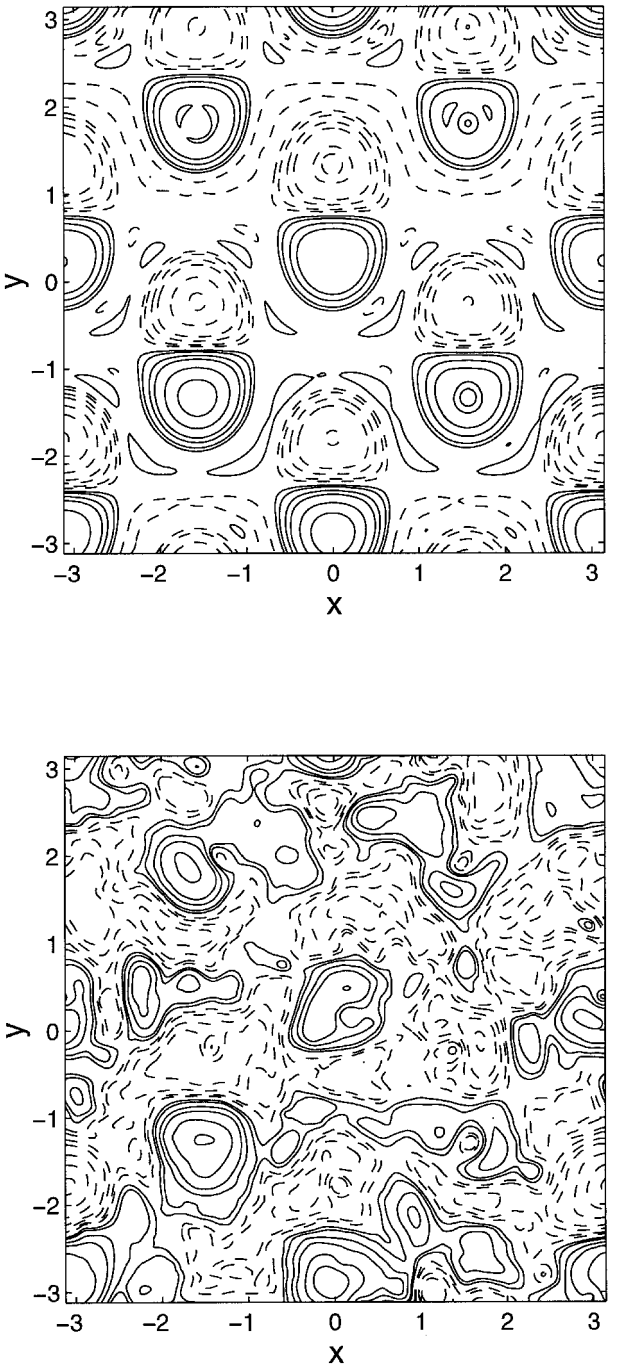

Figure 10. The mean (upper panel) and instantaneous (lower panel) streamfunctions for the cosine bump case. The instantaneous field is from $t = 7.5$. The contour values are [.05, .1, .3, .5, .7, .9].

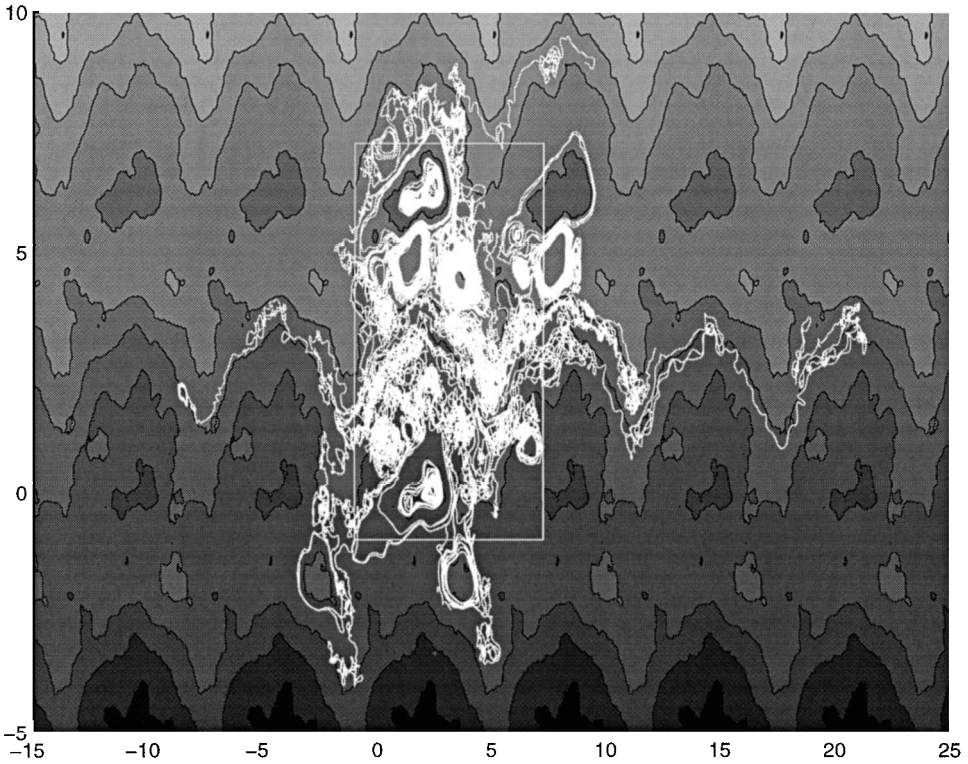

Figure 11. Trajectories for the random bump case, superimposed on f/H.

spreading in x; (as discussed in the Appendix, one could "reset" the ζ displacement after each revolution around a closed contour, but this would obscure the shear dispersion).

Thus this case differs from the previous one because (1) particles can be trapped in closed contour regions and (2) the mean dominates the flow. In turn, spreading along f/H contours is much greater than in either zonal or meridional directions. The dispersion moreover increases quadratically in time, due to the strong mean. However, the topography is still very idealized. Whether such tendencies carry over to more realistic topography is examined next.

6. Random topography

In the last example, we consider dispersion over random topography. Studies freely evolving turbulence over random topography include Bretherton and Haidvogel (1976) and Holloway (1978). As did Bretherton and Haidvogel, we choose a topographic spectrum dominated by the gravest modes and proportional to κ^{-2}, which is similar to the observed topographic spectrum in the ocean. The resulting f/H field, and a subset of the resulting particle trajectories, are shown in Figure (11). Because of the periodic domain, there is a large-scale periodicity in the field, despite the fact that the topography is random.

As in the cosine bumps case, some particles are trapped near closed contours, while others wander in regions of open contours; instances of the latter are less frequent however, presumedly due to the greater areal proportion of closed contour regions. The Cartesian dispersion (Fig. 12) is anisotropic, and dominated by zonal spreading; however, a power law dependence is not clear in either direction. It appears instead that the rate of spreading is gradually decreasing in both directions.

Besides displaying increased anisotropy, the projected statistics (lower panel) suggest simple shear dispersion along the contours. Indeed, the mean flow (not shown) again is dominant, with an rms velocity which is 84% as large as the instantaneous rms velocity. Both measures of dispersion across contours suggest continued spreading, as in the previous examples with topography.

From Bretherton and Haidvogel (1976) and Holloway (1978), we expect the mean flow to have a spatial structure which resembles a low-pass filtered version of f/H (the degree of filtering depends on the total energy). As such, displacements ought to be projected onto a low pass filtered version of f/H rather than to the actual field itself. Doing so[5] yields the dispersion curves in dashed lines in the lower panel of Figure 12, and one observes the cross contour dispersion is further suppressed. The along contour dispersion is not appreciably changed, and is still shear dispersive.

7. Floats

As noted in the introduction, the present results might pertain to particle motion in the deep ocean, below the region of wind forcing. To examine to what extent this is true, trajectories from SOFAR and RAFOS floats deployed in the North Atlantic during the 1970's and 1980's[6] were used to calculate zonal and meridional dispersion, and dispersion projected onto f/H. Only floats deployed below 1000 m (the nominal depth of the thermocline) and which lasted longer than 100 days were used; dispersion up to one year was calculated. All floats were taken together for the calculation, and no normalization (e.g. Rupolo *et al.,* 1996) was made. A more complete discussion of the data, of regional variations and dynamical interpretations are presented in (LaCasce and Speer, 1999).

The trajectories used are shown in Figure 13, superimposed on the f/H field.[7] One can see a general tendency for floats to follow the contours: for example, floats in the eastern Atlantic south of the Azores Plateau tend to spread more zonally than do those to their north, and likewise the contours of f/H are more zonally oriented in the former region.

5. The field is Fourier-transformed in two dimensions, and the high wavenumber components removed with a circular Butterworth filter. The f/H field was filtered to resemble the mean streamfunction.

6. The datasets come from the MODE, LDE, Eastern Basin, EUROFLOAT, ABACO, Canary Basin, Gulf Stream, Gulf Stream Recirculation, Iberian Basin, Long Range, Northeastern Atlantic, PreLDE and Ring experiments. Further information may be found at the WOCE Float Data Archive, http://wfdac.whoi.edu.

7. The f/H field for Figure 13 was calculated using a one degree topographic data set. The f/H field used for the calculations was made using etopo5, a topographic set with $\frac{1}{12}$ degree resolution; horizontal scales smaller than approximately 20 km were smoothed out using a two-dimensional low pass (spectral) filter. A discussion of the sensitivity of the results to smoothing is given in LaCasce and Speer (1999).

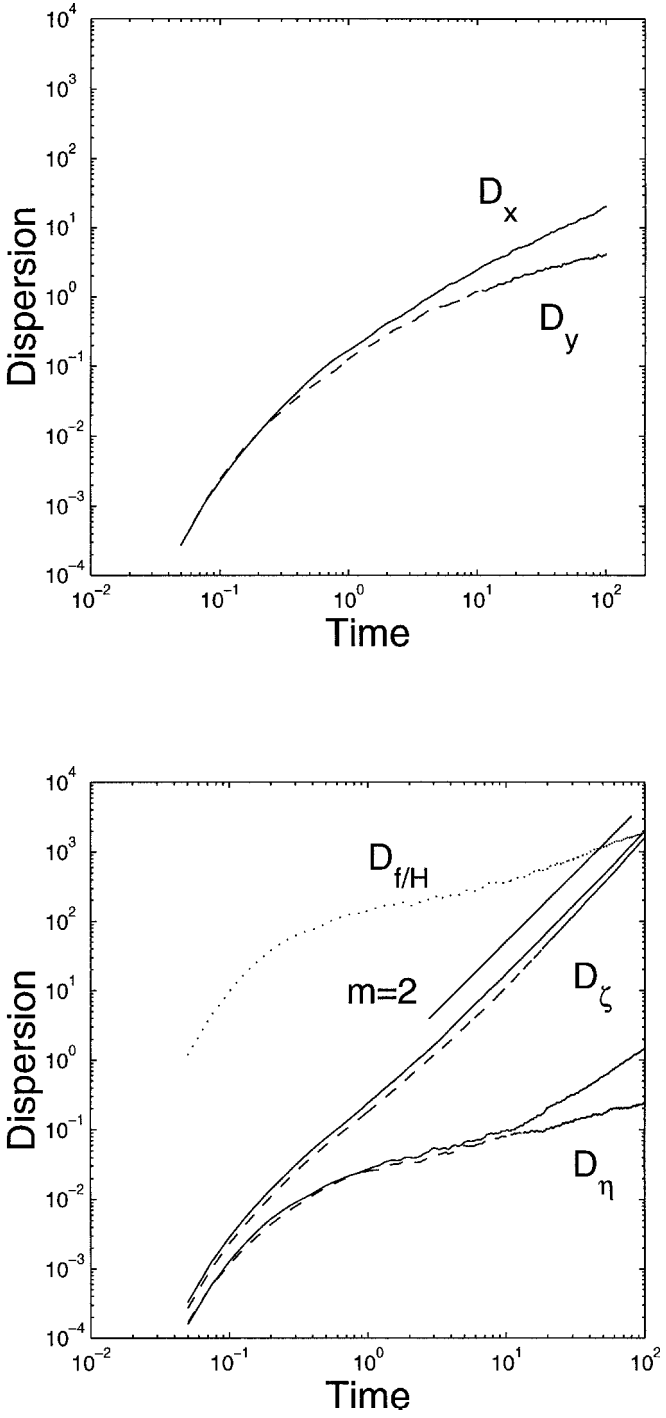

Figure 12. Dispersion in the random bump case. The zonal and meridional dispersion are shown in the upper panel, the dispersion relative to *f*/*H* in the lower panel. The solid lines in the lower figure correspond to dispersion calculated relative to the actual *f*/*H* field, and the curves which are dashed (at early times) relative to a smoothed version of *f*/*H*.

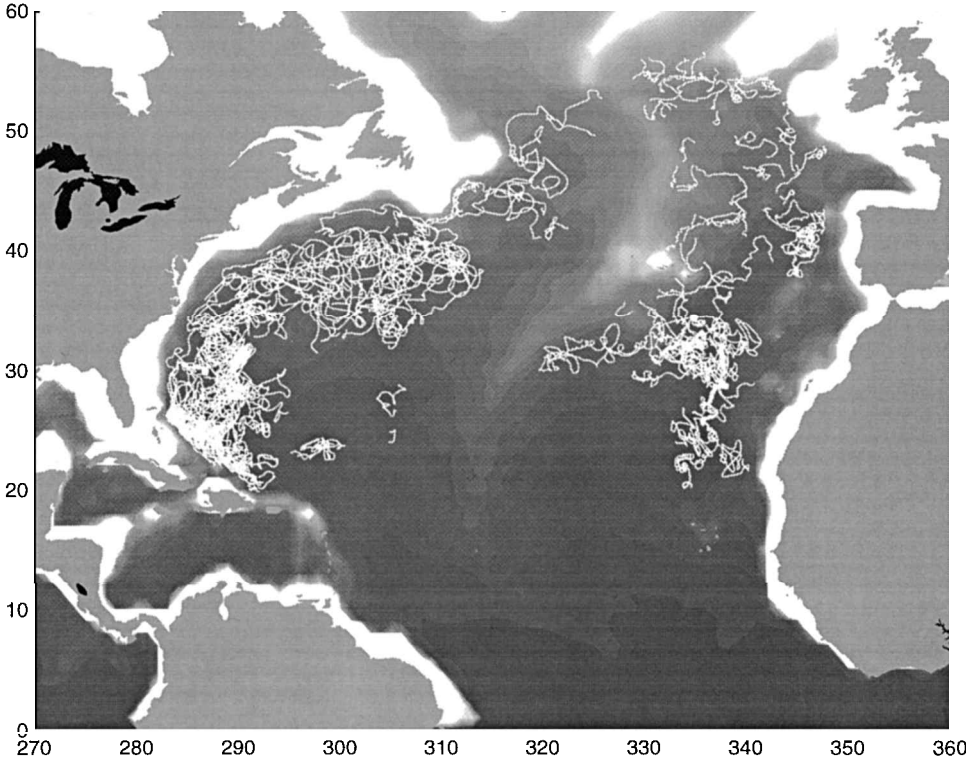

Figure 13. SOFAR and RAFOS float trajectories in the North Atlantic superimposed on the *f*/*H* field obtained from a one degree topographic data set.

The dispersion in Cartesian coordinates is shown in the upper panel of Figure 14, and that calculated relative to the *f*/*H* contours in the lower panel. The lowest curve in both figures represents the number of floats used in the averages; there are about 160 floats initially, but fewer at late times.

The Cartesian dispersion (upper panel) is nearly isotropic and grows approximately linearly in both directions, suggestive of diffusion in isotropic turbulence. In contrast, the dispersion with respect to *f*/*H* is anisotropic from the outset, with the dispersion along contours more than three times greater than across contours. The total cross-contour dispersion is less than that across latitude lines, suggesting a greater resistance to crossing *f*/*H* contours. The increase in dispersion is clearly linear in both directions, from roughly 15 days (a time comparable to the Lagrangian integral time scale) to one year. The results thus suggest diffusion both along and across contours, with a larger diffusion "coefficient" along the contours. The same result is found in the "ridge" case above, i.e. one in which there were no closed contours of *f*/*H*. While there are such closed contours in the North Atlantic, most of the floats are in open contour regions. However, the agreement between data and model may be fortuitous.

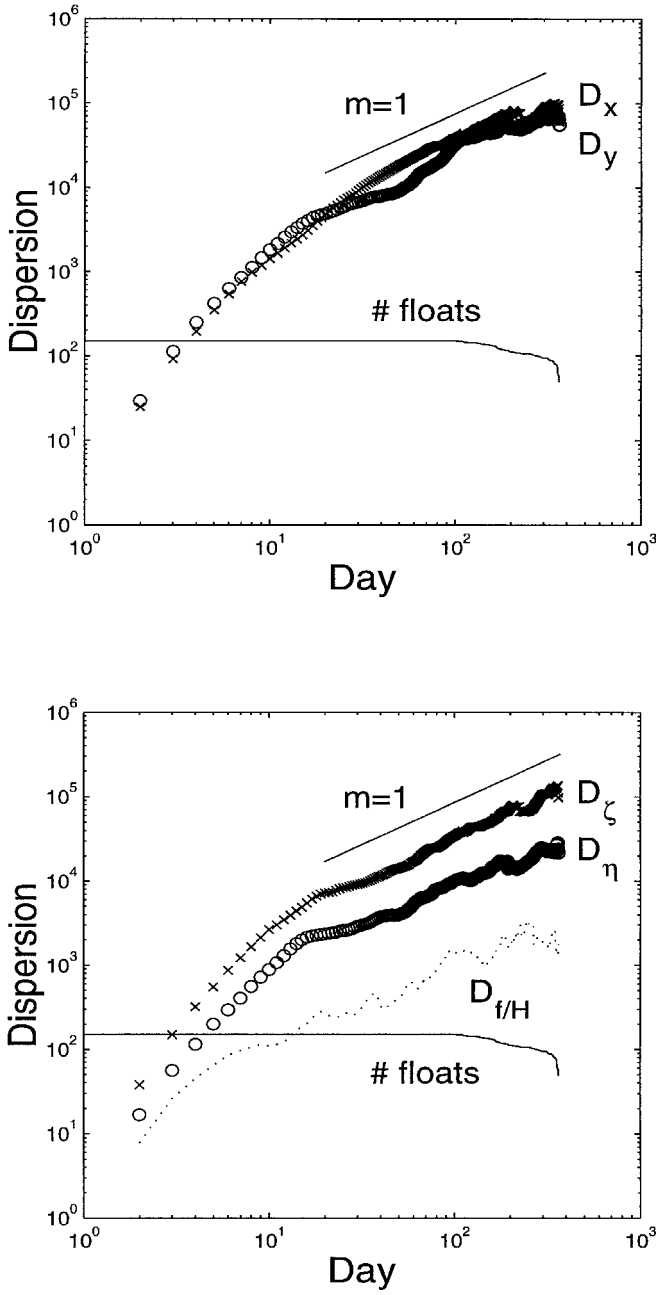

Figure 14. Dispersion for the North Atlantic floats. The zonal and meridional dispersion are shown in the upper panel, the dispersion relative to *f/H* in the lower panel. The 1/12 of a degree etopo5 topographic data set was used, smoothed to remove horizontal scales smaller than approximately 20 km.

Considering subsets of floats only in the west or eastern Atlantic yields the same result. As discussed in the ensuing work (LaCasce and Speer, 1999), the mean displacements are greatest along *f/H*, and indicate a pseudo-westward drift at this depth. We note these results here only as evidence of the relevance of such "projected" statistics; as noted, a fuller discussion of the application to float data is presented in LaCasce and Speer (1999).

8. Discussion

In barotropic flows in which potential vorticity is conserved, particle dispersion is preferentially along lines of *f/H*. Without topography, the spread of particles is greater along latitude lines than across, and this anisotropy is evident when comparing the dispersion in x and y directions. With topography, the *f/H* contours vary in (x, y), and as such the dispersion anisotropy is more clearly evident for displacements along and across contours of *f/H* itself.

In all the present cases, dispersion was more anisotropic relative to *f/H*. The primary difference was between the rates of spreading. In terms of the along-*f/H* spreading, the rate appears to depend on the number of Eulerian components present. In cases with a dominant mean shear flow, or a single Rossby wave, we obtain shear dispersion. If there were several equally strong components, the increase in time was less than quadratic, e.g. in the ridge case, where the increase was linear, consistent with along-contour diffusion. Interestingly, the along-*f/H* dispersion was found to be either shear dispersive or diffusive in these examples, even when the Cartesian measurements were suggestive of "anomalous" diffusion.

In the flat bottom cases considered, the across-*f/H* diffusion ceased after a short period of time; one may argue that this must be so, given the conservation of both potential and relative enstrophy. With topography, the dispersion across contours increased slowly over the duration of the experiment (though we argue that it would eventually cease, given our periodic domain). The rate of increase was at best linear in time, though it was slower in cases with closed contours.

It should be emphasized that projecting displacements onto most *f/H* fields will not preserve distance; in other words, the total dispersion in the *f/H* and Cartesian frames will not in general be equal. A simple example is when particles circle around a closed contour, increasing their net along-contour displacement without really changing their position. Nevertheless, the results can lead to qualitative insight into transport, as well as to possible parameterizations.

As mentioned before, we have used a dissipative numerical model to study how PV conservation affects dispersion. The agreement between the results of the simulation in Section 3 with those of an inviscid, single wave calculation are reassuring. Nevertheless, one must admit the possibility of quantitative changes in the rates of spreading when using much higher resolution models.

Though we have focused on the second moment of the displacements, we have examined the first, third and fourth as well. The most useful of these is the first moment; in the cases with closed f/H contours, the first moment decreased monotonically, consistent with "westward" (relative to f/H) advection by the mean flow described earlier. In cases without mean flows, the mean drift along contours generally depended on the deployment of particles, i.e., how many move "west" as opposed to "east." In all cases the mean displacement across f/H was near zero. We found strong variations in the skewness, with no clear tendencies evident. The kurtosis in general was near the Gaussian value of 3, and could not be used to differentiate runs. In our examination of float data (LaCasce and Speer, 1999), we treat the first and second moments exclusively.

We have examined barotropic and unforced flows, but of course the ocean is baroclinic and forced by the wind. How the present results carry over to such cases will depend on a number of factors, such as the relative importance of barotropic eddies. An obvious baroclinic modification would be to examine the relation to f/H, where h is the depth below the thermocline. Such a study is underway, relative to RAFOS trajectories under the Gulf Stream (Bower, 1997; personal communication).

Lastly, we have presented evidence that floats in the North Atlantic also spread preferentially along contours of f/H. The projected dispersion moreover was found to increase linearly both along and across contours. This suggests that mixing in the deep ocean may be represented as a diffusive process, with an along-contour diffusivity which is greater than the cross-contour diffusivity. This intriguing result will be discussed in more detail in LaCasce and Speer (1999).

Acknowledgments. JHL enjoyed conversations with Russ Davis, Bach Lien Hua, Volfango Rupolo, Steve Lentz, Amy Bower and Glenn Flierl. An anonymous reviewer made a number of useful suggestions as well. Glenn Flierl provided the quasi-geostrophic numerical code, and Audrey Rogerson wrote the particle advection scheme. The etopo5 topographic set is available from the National Geophysical Data Center (http://www.ngdc.noaa.gov). JHL was supported under MAST PL920057 and KGS by the Centre Nationale de Recherche Scientifique.

APPENDIX

Definition of moments

Consider a group of particles moving in (x, y). The mean zonal displacement from their starting positions is defined:

$$M_x(t) \equiv \langle x_i(t) - x_i(t_0) \rangle_i, \tag{11}$$

where the symbol $\langle \ldots \rangle_i$ denotes the average over all particle paths, and M_y is similarly defined. Given different starting positions $x_i(t_0)$, such an average over particle paths is also an average over all starting positions. For spatially homogeneous flows, this approximates an ensemble average, but not for inhomogeneous flows. This is an important distinction in the case of flows with variable topography.

The (absolute) zonal dispersion of the particles is defined:

$$D_x(t) \equiv \langle (x_i(t) - x_i(t_0) - M_x(t))^2 \rangle_i, \tag{12}$$

and the meridional dispersion is similarly constructed. The mean displacement of the particles is removed, so dispersion reflects the growth of the ''cloud'' about the center of mass (with the same comments with regards to the loss of information about spatial inhomogeneities applying). Higher order moments may also be defined:

$$\Gamma_x(t) \equiv \frac{\langle (x_i(t) - x_i(t_0) - M_x(t))^n \rangle_i}{D_x^{n/2}}, \tag{13}$$

where the normalization by the dispersion is traditional. The third order moment is the skewness (S_x, S_y), and the fourth, the kurtosis (K_x, K_y). For a Gaussian distribution of displacements, the higher order moments are predictable from the central limit theorem: the skewness is zero, and the kurtosis is 3 (e.g. Papoulis, 1984).

The particle displacements are projected onto an arbitrary field as follows. Consider a field, $F(x, y)$, and a time series of particle positions $x_f(t)$ and $y_f(t)$:

$$x_f = [x_f(0), x_f(1), x_f(2), \ldots x_f(N)]. \tag{14}$$

One may define the displacements in both directions at each time:

$$\Delta x_f = [x_f(1) - x_f(0), x_f(2) - x_f(1), x_f(3) - x_f(2), \ldots], \tag{15}$$

and a similar expression for Δy_f. The displacements are projected onto the isolines of $F(x, y)$ by taking cross and dot products with the local gradient of $F(x, y)$:

$$\Delta\zeta \equiv (\Delta x_f, \Delta y_f) \times (\nabla F/|\nabla F|), \tag{16}$$

and

$$\Delta\eta \equiv (\Delta x_f, \Delta y_f) \cdot (\nabla F/|\nabla F|), \tag{17}$$

where ζ is the coordinate parallel to the isolines of $F(x, y)$, and η the coordinate perpendicular. The gradient is normalized to preserve the length of the displacement. The positions along and across the curves are then found by summing; i.e. the jth element of the position along the curve is:

$$\zeta(j) - \zeta(t_0) = \sum_{k=1}^{k=j} \Delta\zeta(k), \tag{18}$$

with a similar expression for $\eta(t) - \eta(t_0)$. Note that it makes no difference for the moments that the initial positions are unknown. In the case of particles circling on closed contours, one must make a decision whether to ''reset'' an effective azimuthal angle when calculating distances; for the purposes of this paper, we chose not to. However, one could calculate the

distances taking this into account. In any event, distance in general is not conserved after the projection, or, $D_\zeta + D_\eta \neq D_x + D_y$.

The moments are then constructed as before. For example, the dispersion along isolines is defined:

$$D_\zeta(t) \equiv \langle(\zeta_i(t) - \zeta_i(t_0) - M_\zeta(t))^2\rangle_i. \tag{19}$$

The field used in the present work is the *f/H* field. The statistics thus describe how the particles move relative to the isolines of *f/H*, e.g. whether there is a mean drift, dispersion along/across isolines, etc.

A potential problem with the construction as defined above is that summing the sequence of displacements along and across contours is potentially numerically unstable. Errors introduced at intermediate steps, usually from uncertainties in the field, propagate and affect the net result (e.g. Henrici, 1982). The error magnitude and its growth in time may be estimated as follows. Assuming an error in the position of the float, $(\varepsilon_x(t_i), \varepsilon_y(t_i))$, the displacement array in Eq. (15) may be rewritten:

$$\Delta x_f = [x_f(1) - x_f(0) + \varepsilon_x(1) - \varepsilon_x(0), x_f(2) - x_f(1) + \varepsilon_x(2) - \varepsilon_x(1), \ldots]. \tag{20}$$

Resumming Δx_f yields the original positions, x_f, with the initial position subtracted from each element. The errors recombine similarly, so that position error at each point is the same as the value prior to manipulation, minus the error at the initial position. But projecting the displacements onto the isolines of *f/H* alters the errors; for simplicity, consider only the contribution to the along/across displacement vectors which comes from the dot product with the gradient *f/H* vector:

$$\Delta x_f \cdot (\nabla F/|\nabla F|) \equiv \Delta x_f \cdot n = [(x_f(1) - x_f(0)) \cdot n(1) + (\varepsilon_x(1) - \varepsilon_x(0)) \cdot n(1), \ldots]. \tag{21}$$

The error in the gradient of *f/H* has been ignored; i.e., we assume that this field is known perfectly; a similar analysis is possible when including such an error. In resumming this displacement, adjacent errors no longer cancel, due to the multiplication by n. So one obtains:

$$\sum(\Delta x_f \cdot n) = \sum_{i=0}^{i=j-1}((x_f(i+1) - x_f(i))) \cdot n(i) + \sum_{i=0}^{i=j-1}(\varepsilon_x(i+1) - \varepsilon_x(i)) \cdot n(i). \tag{22}$$

The first term on the RHS is the zonal contribution to $\eta(t_j) - \eta(0)$ in Eq. (17) (a similar term is found for the meridional contribution). The second term is the error. One can gauge the size of this term as follows. The vector, n, is less than or equal to unity, by the normalization, and the magnitude of ε depends on the accuracy of the float position. For model floats, that in turn depends on the accuracy of the particle advection scheme; for actual floats, the error depends on acoustical fixing of the position, etc. For the moment,

call this error magnitude A. Then we have:

$$\sum_{i=0}^{i=j-1} (\varepsilon_x(i+1) - \varepsilon_x(i)) \cdot n(i) \leq \sum_{i=0}^{i=j-1} A\gamma(i), \tag{23}$$

where γ is an error of unit magnitude. Assuming the positional errors are random and normally distributed with zero mean, the contribution to the mean displacement will vanish. However, the dispersion involves squared differences, and so the γ contribution will not vanish. Consider the contribution to the squared cross-*f*/*H* displacement from this zonal part:

$$\eta_x(j)^2 = \sum_{i=0}^{i=j-1} (D(i) + A\gamma(i))^2, \tag{24}$$

where η_x^2 is that portion of the squared cross *f*/*H* displacement due to the zonal contribution, and $D(i) \equiv (\varepsilon_x(i+1) - \varepsilon_x(i)) \cdot n(i)$. Averaging over all particles yields:

$$\langle \eta_x(j)^2 \rangle = \sum_{i=0}^{i=j-1} \langle D^2(i) \rangle + 2A \langle D(i)\gamma(i) \rangle + A^2 \langle \gamma^2(i) \rangle. \tag{25}$$

Assuming the errors in the positions are uncorrelated with the positions themselves (a standard assumption; e.g. Batchelor and Townsend, 1953), the second term on the RHS vanishes and the error is due solely to the third term (with a similar contribution from the meridional displacement portion of η^2). Given a large enough collection of particles, and under the assumption of Gaussian statistics for $\gamma(i)$, we have (e.g. Bendat and Piersol, 1986):

$$\sum_{i=0}^{i=j-1} A^2 \langle \gamma^2(i) \rangle \, \alpha \, (A^2)j, \tag{26}$$

or the error of the squared displacement grows linearly in time. Its magnitude is the square of the position error itself. For the deep Atlantic floats in Section 7, the late time dispersion was also found to increase linearly in time, with a magnitude greater than 10^4 km^2. The squared positional error is generally $O|(1 - 10)$ km$^2|$, so the contribution from the projected errors is much smaller than the magnitude of the displacement itself. A similar comparison for the model data reveals an even greater discrepancy, because the particle position errors are very small.

Nevertheless, one may define a second dispersion which does not suffer from such a propagation of errors. That is the dispersion of the value of the field itself, as sampled by the particle:

$$D_F(t) \equiv \langle (F_i(t) - F_i(t_0) - M_F(t))^2 \rangle_i, \tag{27}$$

where $F_i(t)$ is the value of the field observed by particle i at time t. For the f/H field, this defines $D_{f/H}$. Strictly speaking, this displacement is a more suitable companion for the along contour displacement, ζ, because the displacement defined thus is independent of the local gradient in the field. For example, in a region of strong gradients, a particle may not cross a great distance before experiencing large changes in the mean PV. In regions of weak gradients, the particle may wander over large distances before noticing a change in the mean field. So a measure of the value of the field itself is preferable. However, D_η is more suitable for comparison with D_ζ because both are squared distances, as are the dispersion in zonal and meridional directions. Thus both measures of cross contour spreading have been retained here.

REFERENCES

Batchelor, G. K. and A. A. Townsend. 1953. Turbulent diffusion. Surveys in Mechanics, *23,* 352–398.

Bendat, J. S. and A. G. Piersol. 1986. Random Data: Analysis and Measurement Procedures, John Wiley and Sons, 566 pp.

Bretherton, F. B. and D. Haidvogel. 1976. Two-dimensional turbulence over topography. J. Fluid Mech., *78,* 129–154.

Davis, R. E. 1991. Observing the general circulation with floats. Deep-Sea Res., *38,* (Suppl.), S531–S571.

Fjortoft, R. 1953. On the changes in the spectral distribution of kinetic energy for two-dimensional non-divergent flow. Tellus, *5,* 225–230.

Flierl, G. R. 1981. Particle motions in large-amplitude wave fields. Geophys. Astrophys. Fluid Dyn., *18,* 39–74.

—— 1994. Semicoherent oceanic features. Chaos, *4,* 355–367.

Henrici, P. 1982. Essentials of Numerical Analysis, John Wiley and Sons, 409 pp.

Holloway, G. 1978. A spectral theory of nonlinear barotropic motion above irregular topography. J. Phys. Oceanogr., *8,* 414–427.

—— 1992. Representing topographic stress for large-scale ocean models. J. Phys. Oceanogr., *22,* 1033–1046.

Holloway, G. and S. S. Kristmannsson. 1984. Stirring and transport of tracer fields by geostrophic turbulence. J. Fluid Mech., *141,* 27–50.

Kraichnan, R. H. and D. Montgomery. 1980. Two dimensional turbulence. Reports Progr. Phys., *43,* 547–619.

LaCasce, J. H. 1998. A geostrophic vortex over a slope. J. Phys. Oceanogr., *28,* 2362–2381.

LaCasce, J. H. and K. G. Speer. 1999. Oceanic floats and *f/H*. (in preparation).

Mezic, I. and S. Wiggins. 1994. On the dynamical origin of asymptotic t^2 dispersion of a nondiffusive tracer in incompressible flows. Phys. Fluids, *6,* 2227–2229.

Papoulis, A. 1984. Probability, Random Variables and Stochastic Processes, McGraw-Hill, 576 pp.

Pedlosky, J. 1987. Geophysical Fluid Dynamics, Springer-Verlag, 710 pp.

Pierrehumbert, R. T. 1991. Chaotic mixing of tracer and vorticity by modulated traveling Rossby waves. Geophys. Astrophys. Fluid Dyn., *58,* 285–319.

Regier, L. and H. Stommel. 1979. Float trajectories in simple kinematic flows. Proc. Natl. Acad. Sci. USA, *76*(10), 4760–4764.

Rhines, P. B. 1975. Waves and turbulence on a beta-plane. J. Fluid Mech., *69,* 417–443.

—— 1977. The dynamics of unsteady currents, *in* The Sea, Vol. *6,* Interscience, 189–318.

Rupolo, V., B. L. Hua, A. Provenzale and V. Artale. 1996. Lagrangian velocity spectra at 700 m in the western North Atlantic. J. Phys. Oceanogr., *26,* 1591–1607.

Solomon, T. H., E. R. Weeks and H. L. Swinney. 1993. Observation of anomalous diffusion and Levy flights in a two-dimensional rotating flow. Phys. Rev. Lett., *71,* 3975–3978.

Taylor, G. I. 1921. Diffusion by continuous movements. Proc. Lond. Math. Soc., *20,* 196–212.

Vallis, G. K. and M. E. Maltrud. 1994. Generation of mean flows and jets on a beta-plane and over topography. J. Phys. Oceanogr., *24,* 2305–2326.

Weiss, J. B. and E. Knobloch. 1989. Mass transport by modulated traveling waves. Phys. Rev., *A40,* 2579–2589.

Received: *10 March, 1998;* revised: *19 October, 1998.*